Supplemental Document

SI-traceable molecular transition frequency measurements at the 10^{-12} relative uncertainty level: supplement

Z. D. Reed,* D. A. Long, H. Fleurbaey, and J. T. Hodges

Chemical Sciences Division, National Institute of Standards and Technology, 100 Bureau Drive, Gaithersburg, Maryland 20889, USA
**Corresponding author:* *zachary.reed@nist.gov*

Supplement DOI: https://doi.org/10.6084/m9.figshare.12702395

Parent Article DOI: https://doi.org/10.1364/OPTICA.395943

Supplemental Materials

Molecular transition frequency measurements at the 10^{-12} relative uncertainty level

ZACHARY D. REED*, DAVID A. LONG, HÉLÈNE FLEURBAEY, JOSEPH T. HODGES

Chemical Sciences Division
National Institute of Standards and Technology
100 Bureau Drive, Gaithersburg, Maryland 20889
*zachary.reed@nist.gov

1. Introduction

The Supplemental Materials comprise 1) a description of the comb-locked cavity ring-down spectrometer and data processing methods, 2) the spectral modeling and fitting procedure with a discussion of impact on fitted molecular line centers, 3) experimental results of varying spectral density, 4) a discussion of the shifting terms and their uncertainty, 5) a description of the Monte Carlo simulations performed and the corresponding results, 6) a characterization of the comb-locked laser, including laser linewidth, frequency stability, and power spectral density, and 7) a comparison to previously reported CO_2 line positions.

2. Experimental Description

The optical cavity consists of two highly reflective mirrors separated by nominally 140 cm with intensity reflectivity R=0.999 976 at the probe laser wavelengths employed here. The external cavity diode probe laser (ECDL) has a wavelength tuning range of 1570 nm to 1630 nm and a high-bandwidth DC-coupled external input for control of the diode current. The laser power is amplified with a fiber amplifier to approximately 25 mW. The optical frequency comb (OFC) is a Menlo Systems FC1500 self-referenced, octave-spanning system with a 250 MHz repetition rate and a carrier-envelope offset of 20 MHz. The OFC is actively locked to a Cs clock (Microsemi 5071A), with a relative frequency stability of approximately 10^{-14} for an averaging time of 5 days. All samples were static charges of isotopically enriched $^{12}CO_2$ (99.99%) which was allowed to stabilize in the optical cavity overnight to improve the pressure stability.

Ring-down decay signals are digitized at 10 MSamples s^{-1} at 16 bits of resolution, with the time-dependent decay signal $s(t)$ modeled using the conventional CRDS equation

$$s(t) = s_0 \exp(-t/\tau(\nu_q)) + s_b \quad \text{(S1)}$$

where ν_q is the optical frequency corresponding to mode q, τ is the intensity decay constant, s_0 is the decay signal amplitude, and s_b is a constant offset corresponding to the base mirror losses.

The spectrum of total loss per-unit-length is therefore modeled by

$$\frac{1}{c\tau(\nu_q)} = \alpha(\nu_q) + \frac{L_0(\nu_q)+\Delta L_{et}(\nu_q)}{l} \quad \text{(S2)}$$

where c is the speed of light, l is the mirror-to-mirror distance, L_0 = 1 - $(R_1R_2)^{1/2}$ is the effective mean cavity mirror loss given the two mirror reflectivities (i.e., R_1 and R_2), ΔL_{et} is the loss contribution of etalons which are manifest as sinusoidal variations in the base losses (if present), and α is the absorption coefficient of the sample. The etalon amplitude and period are determined from measurements with an evacuated cavity and subsequently fixed. Additionally, we have corrected for non-ideal digitizer linearity using the procedure recently described in Fleisher et al. [1], where the measured τ_A is corrected by $\tau = b_1\tau_A + b_0$, where b_1 and b_0 are empirical coefficients resulting from the digitizer calibration. This results in loss spectra modeled by

$$\frac{1}{c(b_1\tau_A(\nu_q)+b_0)} = \alpha(\nu_q) + \frac{L_0(\nu_q)+\Delta L_{et}(\nu_q)}{l} \quad \text{(S3)}$$

The temperature is determined with a NIST-calibrated platinum resistance thermistor with a standard uncertainty of 20 mK imbedded in the wall of the CRDS cell. The temperature is recorded at each spectral point, with the mean employed for subsequent calculations. The room temperature is tightly regulated, with no additional temperature controls on the cell itself. Temperature drifts on the order of 10 mK are typically observed in the time period of one spectral acquisition. Gradients on the order of 10 mK are observed along the longitudinal axis of the cell. More extensive discussions of temperature determinations in this cell may be found in [2, 3].

3. Typical Spectrum Results

Figure S1a shows a representative spectrum of the P10e transition of the (30012) ← (00001) band of $^{12}C^{16}O_2$ at a pressure of 0.70 Pa and nominally 296.6 K. A spectral bandwidth of 6.5 GHz was measured, which is sufficient to capture the Doppler-limited absorption profile. In this case, spectral intervals were equal to the free spectral range (FSR) of the optical cavity, resulting in a spectrum with 60 spectral points. A total of 100 ring-down decay signals were acquired per spectral point, resulting in an acquisition time of roughly 100 s. A nearly Doppler-limited Voigt profile can be fit to the measured absorption profile with good fidelity (as evidenced by no systematic residuals and no evidence of asymmetry) by floating the Doppler width, line center, and line area. The calculated Lorentzian width based on the HITRAN 2016 broadening coefficient (32.25 MHz/kPa) for this self-broadened transition was used when fitting the spectra [4]. The signal-to-noise ratio (SNR), defined as peak losses over the root-mean-square of the baseline residuals, is nearly 14 000:1. All fitted parameter uncertainties reported are calculated by the fitting program. The fitted Doppler width is in generally good agreement with the expected value determined by the thermistor, showing an average deviation of +0.026% with a fit uncertainty of 0.014%. This deviation is within the combined uncertainty of the thermistor and the fitted Doppler width, and also incorporates the average 10 mK drift in the temperature of the cell during the measurement. Systematically decreasing the laser power reduces the fitted Doppler width to within +0.0086% of the calculated value, indicating some broadening of the line profile due to slight residual saturation. This is, however, symmetric and should have no effect on the retrieved line center. Transitions within ±5 GHz of the target with an intensity ratio ($S/S_{interference} > SNR$) were fitted using parameters from HITRAN 2016 to mitigate potential systematic asymmetry [4]. No residual structure was observed from interfering transitions after fitting.

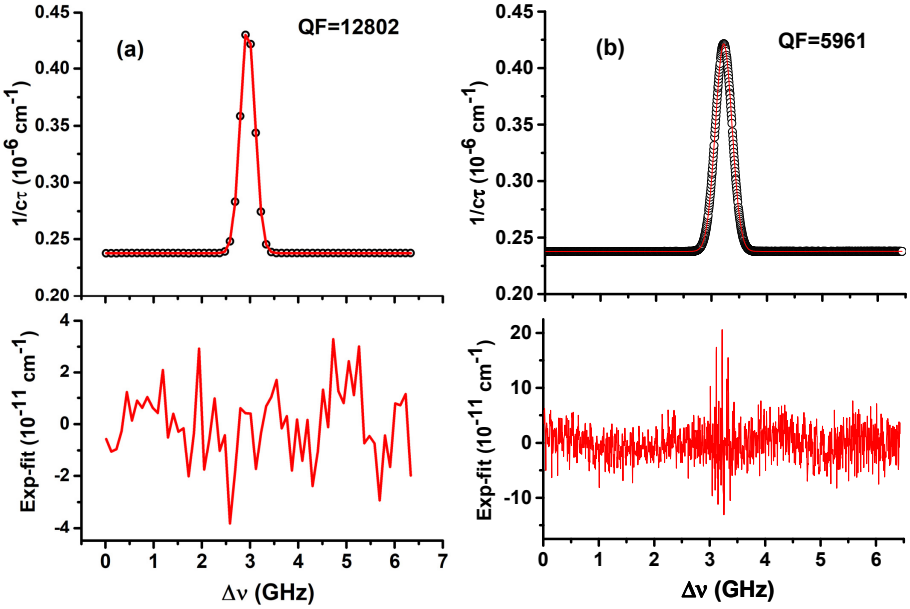

Fig. S1 (a) Typical single-spectrum CL-CRDS at a pressure of p = 0.70 Pa and T = 296.6 K of the P10e $^{12}C^{16}O_2$ (30012) ← (00001) transition, with a spectral sampling density of 107 MHz. Lower pane, spectral residuals of the Doppler profile fit (b) CL-CRDS spectrum of the P10e transition with a spectral sampling density of 5 MHz. Lower pane, spectral residuals of the Doppler profile fit, with individual spectrum baselines fitted. QF is defined as $\mathrm{QF} = (\alpha_{\max} - \alpha_{\min}) / \bar{S}_R$ where $\bar{S}_R$ is the root mean square of the spectral residuals.

4. Measurements at high spectral point density

A spectrum of the $^{12}C^{16}O_2$ P10e transition, recorded at a spectrum point density of 5 MHz can be found in Figure S1b. This spectrum was constructed from 22 separate spectra, each taken at unit-FSR spectral intervals, with each spectrum shifting f_{offset} by 5 MHz. The frequency of each spectrum point is determined directly, while keeping the heterodyne beat signal (f_{beat}) fixed and adjusting f_{offset} and f_{EO}. This approach allowed for the spectra to be interleaved with no increase in frequency axis uncertainty when compared to the non-interleaved case. Some systematic structure is present in the fitted residuals, which are caused by well-known changes in base losses as the cavity length is tuned and slightly different regions of the ring-down cavity mirrors are sampled. Because these spectra are independently measured prior to interleaving, the variations in base loss may be treated as independent baselines. In practice, linear baselines for each component spectrum are individually subtracted prior to the combined fit to the set of $\alpha_n(\nu_q)$, where n represents each independent baseline-subtracted spectrum. This baseline subtraction and interleaving improves the SNR of the fits by nearly 50 %, while significantly reducing the systematic residuals.

To characterize the impact of spectrum point density, we compared the fitted line centers and Doppler widths along with their corresponding uncertainties for the two cases described. The results are largely equivalent, within the reported uncertainties. The temperature-normalized Doppler widths determined for the 107 MHz and 5 MHz spectral densities differ fractionally by 4×10^{-5}, with relative uncertainties of 0.085 % and 0.011 %, respectively. The reported single-spectrum line center uncertainties are 20 kHz and 5 kHz for the two respective cases. The reported fitted line area uncertainties are 0.0098 % and 0.0034

%, respectively. We note that although the 5 MHz spectral density case has lower reported uncertainties, it consists of nearly 1300 spectral points distributed among a family of $n = 22$ interleaved spectra, compared to 60 spectral points in a single spectrum for the FSR case. If an equivalent number of spectra were recorded at the FSR spectrum point density without shifting f_{offset}, the resulting uncertainty would be reduced by the factor $1/\sqrt{n}$, given a result equivalent to the interleaved case. This indicates that absorption profiles which may appropriately modeled by a Doppler profile can be fully described at our 107 MHz FSR spacing at these exceptional SNR levels and do not benefit from increasing spectral sampling.

5. Analysis of Measurements:

Weighting each datum by the inverse of the variance of the measurement uncertainty $\frac{1}{u_i^2}$ reported by the spectrum fitting algorithm, we compute the weighted mean line center as $\bar{f}_0 = (\sum \nu_i/u_i^2)/(\sum 1/u_i^2)$, with a standard uncertainty $u(\bar{\nu}_0) = (1/\sum 1/u_i^2)^{1/2}$.

6. Determination of shifting terms and corresponding uncertainty

The pressure and corresponding pressure shifting terms, were determined individually for each unique spectrum. The CO_2 partial pressure was determined as $p = A\,(k_B T)/(S c)$ where $A = \int \alpha(f) df$ is the integrated line area, S is the line intensity, T is the measured temperature, c is the speed of light and k_B is the Boltzmann constant. The reported uncertainty for A, S, and T are below 0.01%, below 0.1% [5], and nominally 0.02%, respectively, leading to a quadrature sum of nominally 0.1% total uncertainty on the CO_2 pressure determination.

The air pressure, from slight leaks into the cell, was determined for each spectrum by simultaneously recording the cell pressure with a NIST-calibrated capacitance manometer and taking the first spectrum pressure as $p_{air} = 0$, with any increases attributed to leaks. At five days (the maximum time between cavity evacuation and unique sample fills), a maximum air pressure of 1 Pa was observed. The uncertainty contribution from δf_{air} is noted in Table 1 of the main text as "Maximum shift from leaks (over 5 days)."

We calculated the total pressure shift for each individual spectrum based on the sum of three contributions; self-shifting by CO_2 and foreign shifting by residual air (from leakage) and water vapor. The total shift is given by

$\delta f = \left(\delta_{CO2}^{(0)} + \delta'_{CO2}\Delta T\right)p_{CO2} + \left(\delta_{air}^{(0)} + \delta'_{air}\Delta T\right)p_{air} + \delta_{H2O}^{(0)}\, p_{H2O}$, in which the partial pressures of CO_2, air and H_2O are p_{CO2}, p_{air}, and p_{H2O}. Here $\delta_{CO2}^{(0)}$, $\delta_{air}^{(0)}$, and $\delta_{H2O}^{(0)}$ are published values [6, 7] for the pressure-shifting coefficients at the reference temperature T_r = 296 K, $\Delta T = T - T_r$ and δ'_{CO2} and δ'_{air} are the corresponding temperature derivatives of the pressure shifting coefficient. No temperature correction for the H_2O-induced shift was included. The uncertainty components for each shifting term are given by,

$$u_{CO2}(\delta f) = p_{CO2}\delta_{CO2}\sqrt{(u(\delta_{CO2})/\delta_{CO2})^2 + (u(p_{CO2})/p_{CO2})^2 + [(u(\delta'_{CO2})\Delta T)^2 + (\delta'_{CO2}u(\Delta T))^2]/\delta_{CO2}^2},$$

$$u_{air}(\delta f) = p_{air}\delta_{air}\sqrt{(u(\delta_{air})/\delta_{air})^2 + (u(p_{air})/p_{air})^2 + [(u(\delta'_{air})\Delta T)^2 + (\delta'_{air}u(\Delta T))^2]/\delta_{air}^2},$$

and $u_{H2O}(\delta f) = p_{H2O}\delta_{H2O}\sqrt{(u(\delta_{H2O})/\delta_{H2O})^2 + (u(p_{H2O})/p_{H2O})^2}$.

The preceding three components are added in quadrature to give the total uncertainty in the shift as, $u(\delta f) = \sqrt{u_{CO2}^2 + u_{air}^2 + u_{H2O}^2}$.

We calculated the susceptibility to DC Stark shift based on the change (between upper and lower states) in the vibrational component of the static molecular polarizability as discussed by Cai et al. [8]. For the upper state, we obtain $\alpha_v = 1.57\times10^{-41}$ C m^2 V^{-1} and $\Delta\alpha_v = 4.72\times10^{-41}$ C m^2 V^{-1} for the isotropic and anisotropic polarizability components, respectively. Using the corresponding ground-state polarizability values given in [8], we estimate a shift of $\delta f = 1.3 \times 10^{-8} E_f^2$ Hz m^2 V^{-2}, where E_f is the strength of the static electromagnetic field. In comparisons of two Sr optical lattice clocks involving high-finesse optical resonators [9], relative frequency shifts at the 10^{-13} level were observed, which were ascribed to static charge buildup on the cavity mirrors causing field strengths of ~ 30 kV m^{-1}. Treating this value as an upper bound on the strength of stray fields in our cavity, we estimate a DC Stark shift of ≈10 Hz for the R16e transition. To estimate the magnitude of the AC Stark shift caused by an intracavity optical field of amplitude, E_c, we used the approach of Burkart et al. [10] who measured $^{12}C^{16}O_2$ transition frequencies within the (30013) ← (00001) band. They used the quadratic scaling relation of the frequency shift with the field strength derived by Rahn et al. [11] and an approximate value for the polarizability from the CO_2 refractive index, obtaining $\delta f = -1.17 \times 10^{-7} E_c^2$ Hz m^2 V^{-2}. Based on this relation and measurements of circulating power (55 mW) and mode size (0.48 mm $1/e^2$ waist radius) in our ring-down cavity, we calculate an AC Stark shift of -7 Hz. Added together, the AC and DC Stark shifts are nominally 3 Hz.

We also investigated the possibility of Doppler shifting caused by the moving cavity mirrors. Both first- and second-order effects were considered. Given the small amplitude and slow rate of the mirror displacement (0.052 nm and 10 Hz, respectively), the calculated first-order Doppler shift of the incident light is only 1.3 mHz. Further, no deviations from exponential behavior were observed in the fitted residuals of the decay signals, indicating that the induced mirror motion does not introduce appreciable Doppler-shifting. This is consistent with observations from [12], where mirror velocities were more than 10^4 times larger than in our experiment. They observed non-exponential decays caused by Doppler shifting inducing changes in the peak absorption coefficient on the order of 2×10^{-10} cm^{-1} and leading to a fitted line center bias of 362 kHz. For our experiment, their result places an upper bound on the determined line centers from the first-order Doppler shift of 9 Hz.

The second-order Doppler shift, was calculated as $\delta f = -\frac{<v_z^2>}{2c^2} f_0$, in which $< v_z^2 >= k_B T/m$ is the mean-square of the gas velocity component along the cavity optical axis, where T and m are the measured mean gas temperature of each spectrum, and molecular mass of $^{12}C^{16}O_2$. We obtain a value of nominally -59 Hz, with an uncertainty below 0.05 Hz, limited by our knowledge of the sample temperature. This correction was applied to each spectrum based on the mean temperature.

The black-body radiation shift has not been observed for molecular species at 1.6 μm and is expected to be small [13].

7. Monte Carlo simulations

To further investigate statistical (Type A) uncertainties and potential bias (Type B) in the fitted line positions, we performed a Monte Carlo numerical study simulating our experimental spectra with noise sources along both the detuning and absorption axes. The

simulation assumed a Doppler profile at the experimental conditions, the actual spectrum interval (107 MHz) and the number of decays averaged at each point (200). As in our analyses of experimental spectra, six floated parameters were considered in the least-squares fitting algorithm: line center, Doppler width, peak area, baseline loss, slope in baseline loss, and etalon phase. The etalon amplitude and period are determined from empty cavity measurements and subsequently fixed. At each spectrum point, we added uncorrelated Gaussian noise (with a standard deviation consistent with that of the measured spectrum base losses) to the total loss, and we assumed that the triangle-wave dither of the cavity length randomly sampled all laser frequencies within a specified interval relative to the Lorentzian-profile probe laser spectrum. This frequency interval was determined by the cavity length dither width, the offset of the dither lock point relative to the laser line center, and the trigger threshold for the CRDS ring-down events. For zero lock offset, this scheme symmetrically samples the laser spectrum and on average leads to zero bias in fitted line centers. Assuming a relatively large dither lock offset to the cavity mode position of 10 kHz (far greater than what we estimate for our experiment) leads to biases in fitted line center less than 5 Hz, suggesting that there was negligible bias from the lock offset. Assuming zero lock offset and a noise-free baseline, the Type A uncertainty in the fitted line center caused by the cavity length dither is ~7 Hz. Our Monte Carlo simulations also reveal the measured 10 mK temperature excursions introduce a small asymmetry in the measured profile resulting in positive- and negative-going biases in the fitted line center of approximately 150 Hz. However, we find that the principal factor limiting the Type A line position measurement uncertainty is the noise in the spectrum baseline losses. Our calculations predict that uncertainty in the fitted line center for a single spectrum is inversely proportional to SNR and equals ~13.5 kHz for a SNR of 10 000:1. As can be seen in Fig. 6, these calculations are in good agreement with our measurements of SNR for the various lines studied and the associated uncertainties in fitted line position. For statistically stationary behavior and after averaging results, the standard uncertainty for the line position is given by $u(\nu_0) \sim 135$ MHz $(1/\mathrm{SNR})\times(1/n^{1/2})$ where n is the number of fitted spectra and independent determinations of line center. At a spectrum SNR of 10 000:1, we estimate the Type A uncertainty to be less than 1 kHz after averaging 200 spectra (roughly six hours for our measurement acquisition rate). In general, we note that for a purely Doppler-broadened profile limited by Gaussian noise along the absorption axis, provided that $\Delta f < \sigma_D$, our numerical study shows that uncertainty in the fitted line center for a single spectrum is $u(f_0) = (\sigma_D/\mathrm{SNR})\,(\Delta f/\sigma_D)^{1/2}$, where σ_D is the standard deviation of the Doppler profile and
Δf is the experimental spectral sampling interval. This result shows that there is no inherent advantage to oversampling the spectrum for a purely isolated Doppler profile.

8. Influence of the Comb-Lock Servo on the Probe Laser Frequency Spectrum

To demonstrate the degree to which the phase-locking servo transfers the properties of the OFC to the probe laser, and subsequently quantify the effect of the phase-locking servo on the stability and linewidth of the probe laser, we measured the optical frequency spectrum of the probe laser as well as the frequency spectrum and frequency-noise spectral-density (NSD) of the heterodyne beat signal between the OFC and probe laser. Measurements of all three quantities were made under free-running and comb-locked conditions. We note that MHz-level drift in the optical emission from the free-running laser was eliminated using a low-bandwidth proportional-integral-derivative (PID) servo against the wavemeter.

We measured $f_{\mathrm{beat}} = 30$ MHz between the probe laser and OFC and measured the frequency content with a radiofrequency spectrum analyzer (RSA). The beat was implemented prior to launching the beam into free space, subsequent to the electro-optic modulator (EOM) and fiber amplifier. The beat signal was measured with $f_{EO} = 15$ GHz, to provide a beat against a significant different comb mode order from the servo signal. These

measurements (see Fig. S2) show that the phase-locking servo leads to a dramatic narrowing of the heterodyne beat spectrum and thus a high degree of coherence between the probe laser and OFC. The RF beat of the free-running, unlocked laser with the OFC has a half-width at half-maximum (HWHM) of 660 kHz (resolution bandwidth (RBW) = 100 Hz). Setting the RSA to sufficiently short integration times (i.e., sub-ms values) reveals a time-varying narrow spectrum which overlaps (on average) with the spectral contour in Fig. S3. In contrast, for the comb-locked case, the RSA spectrum of the heterodyne beat signal does not vary with time and is dominated by a narrow peak centered on the setpoint heterodyne beat frequency. With the RSA (which is synced to the Cs clock) set at its minimum resolution bandwidth of 0.1 Hz, we measured the linewidth of the heterodyne beat signal traces acquired over several minutes and found a maximum frequency variation about the local oscillator (LO) value of less than ±5 mHz. These results show that the nominally 100-kHz-bandwidth servo used here provides an extremely robust and precise phase-lock of the probe laser to an OFC tooth, whereby the high frequency stability (as well as phase noise) of the OFC is transferred to the probe laser. Subtracting the noise floor (obtained by blocking the optical signal) and integrating the noise yields a residual phase error of 483 mrad, demonstrating that the probe is phase-locked to the OFC.

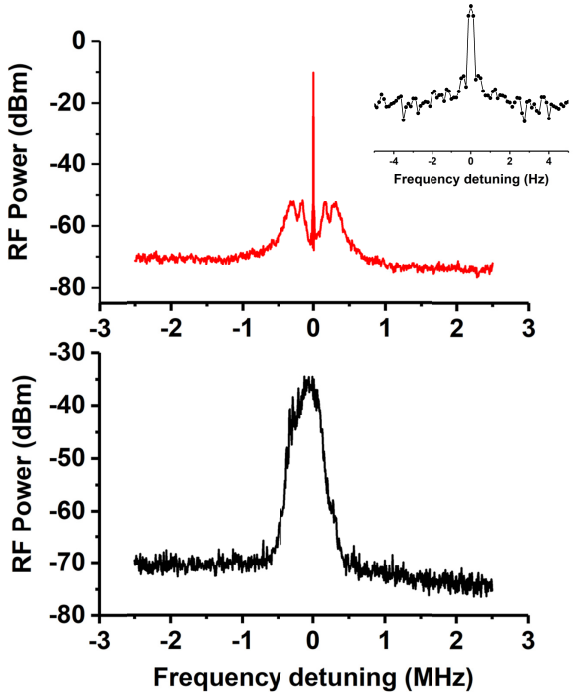

Fig. S2 Swept spectrum analyzer trace of the beat signal (RBW=0.1 Hz) between the OFC and the comb-locked laser (top pane) and the free-running ECDL (RBW=100 Hz) (bottom pane). Inset, expanded view of the comb-locked laser showing tight locking to OFC.

We also used the RSA to measure the NSD of the heterodyne beat signal, which can be found in Figure S3, where we synchronized the time base of the RSA to the 10 MHz Cs-clock to which the OFC is referenced. We find significant reduction in the NSD over the frequency range under the servo bandwidth. The NSD is below the "beta-line separation criteria," $8\ln(2)f/\pi^2$ [14] at all frequencies above 100 Hz. The integrated linewidth derived

from this measurement is driven by the inclusion of the side peaks characteristic of the servo bandwidth (see Fig S2, top pane). This yields the effective bandwidth of the servo, here, nominally 150 kHz depending on servo gain.

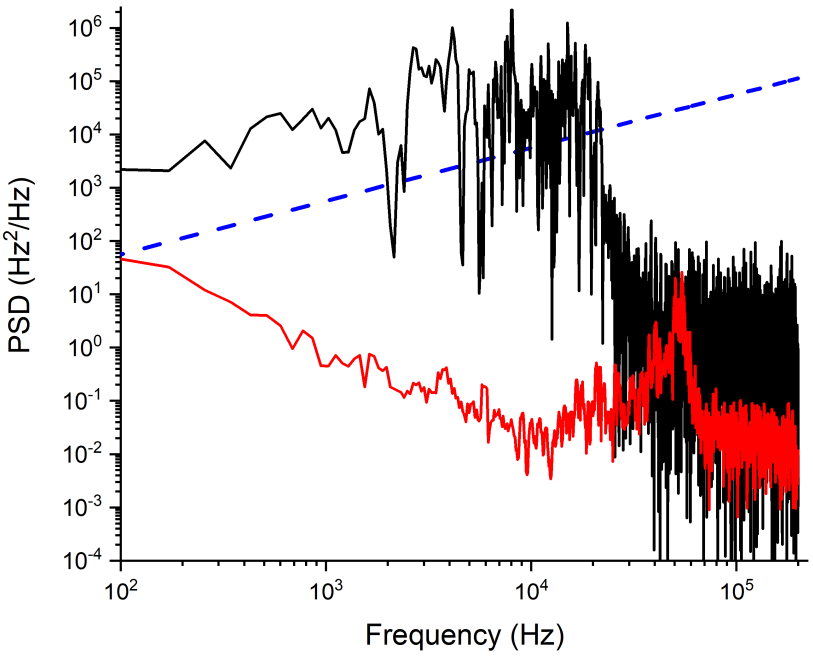

Fig. S3 Frequency noise spectral density of the OFC beat signal of the free-running ECDL (black trace) the out-of-loop comb-locked ECDL (red trace) measured on a RF spectrum analyzer (RBW=100 Hz). The blue dashed line is the beta separation criteria (see text).

The probe laser optical frequency spectra were obtained two ways. The first approach was based on the delayed self-heterodyne interferometric (DSHI) technique [15]. For a DSHI measurement, the laser beam is divided into two paths, one of which is delayed, and the two beams are frequency shifted prior to recombination at a photodetector where the heterodyne beat signal is measured with the RSA. In the present experiment, each beam was frequency shifted with an acousto-optic modulator (AOM), with the delayed beam propagating through a 4 km-long single-mode delay line (delay time $t_d \sim 20$ μs and frequency resolution $\Delta\nu \sim 16$ kHz). Both AOMs were driven by phase-locked RF sources near 50 MHz and separated by 400 kHz. The frequency spectra of the self-heterodyne signal (see Fig. S2) for both free-running and comb-locked cases were obtained by processing the DSHI signal with the RSA at a RBW of 10 Hz. Dividing by a factor $\sqrt{2}$ to account for the fact that the DSHI spectra involve heterodyne beat signals between two incoherent beams, these spectra reveal that the free-running laser has a HWHM linewidth of approximately ~38 kHz, which is significantly reduced (resolution limited) when the laser is locked to the OFC. We also find modulation-induced sidebands on the locked laser spectrum near 100 kHz, which is close to

the PI corner frequency of the servo loop filter. The relatively narrow feature (centered on the spectrum and found only for the comb-locked case, see Fig. S4), provides evidence of coherence in the locked laser persisting on time scales exceeding the optical fiber delay time.

We also quantified the comb-locked probe laser linewidth by measuring the Fourier spectrum of the heterodyne beat signal between this laser and a single-frequency fiber laser having a reported instantaneous linewidth of less than 0.1 kHz. Although the resulting spectrum is noisier than that produced by the DSHI method, we obtain a HWHM of ~17 kHz at 10 Hz RBW, limited by frequency noise on the fiber laser. These methods set an upper bound on the optical linewidth of the probe laser and demonstrate that significant narrowing is achieved.

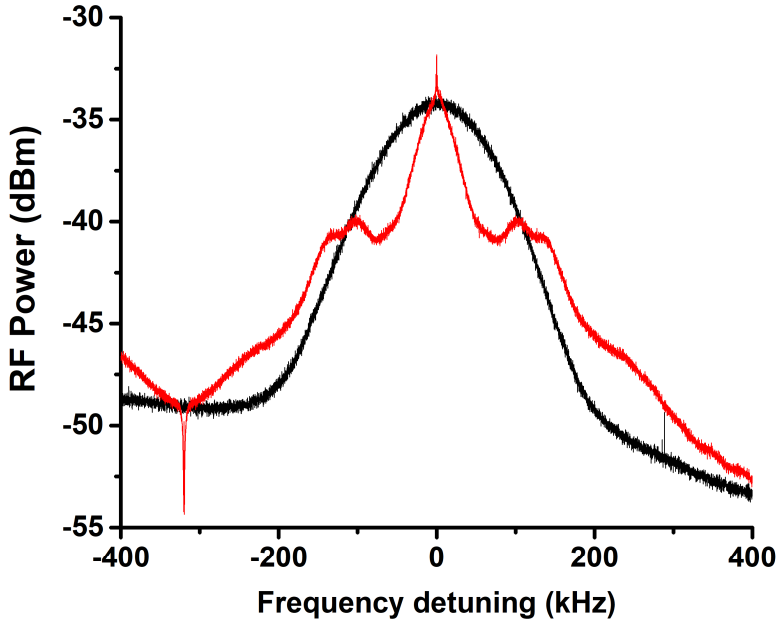

Fig. S4 Electrical spectrum of the self-heterodyne beat signal for the free-running ECDL (black trace) and the comb-locked (red trace)

9. Measurement Statistics for the Heterodyne Beat Signal and Cavity Decay Time

The large enhancement of relative coherence between the probe laser and OFC also yields substantial reduction in the heterodyne beat signal uncertainty, $u(f_{\text{beat}})$. To quantify this effect, we characterized the long-term frequency stability of the phase-lock by continuous measurement of the out-of-loop heterodyne beat signal with the frequency counter set to a 1 s gating time. The free-running (with a low bandwidth wavemeter lock) laser exhibits a slow drift of 700 kHz over a nearly 3 h measurement interval, with short-term deviations of ~100 kHz. The Allan deviation for this case, seen in Figure S5, has a value of 40 kHz at 1 s of averaging, with a minimum occurring after only 10 s. In contrast, the comb-locked laser has an Allan deviation of 400 mHz after 1 s and decreases by a factor of 5 to a minimum of 80 mHz after 60 s of averaging. Thus, the comb-locked probe laser provides at least five orders-of-magnitude improvement in the precision of f_{beat}, compared to that of the unlocked laser. Additionally, comparison of the servoed heterodyne beat signal frequency relative to the LO frequency provides a test of well-known effects of counter offset bias caused by variations in

signal strength and SNR. Based on the time-base-synchronized RSA measurements described above, the mean frequency offset of the heterodyne beat signal relative to the setpoint LO frequency is less than 0.1 Hz, demonstrating that the OFC-locked laser converges to the LO frequency. No frequency drifts are observable at this resolution, indicating that the locked laser effectively reproduces the mean frequency of the OFC tooth over timescales up to several days. Additionally, we repeatedly determined the absolute frequency by recording the comb repetition rate (f_{rep}), carrier-envelope offset (f_{CEO}), and f_{beat}, with 60 s of averaging time for each. The standard errors for f_{rep} and f_{CEO} were 22 μHz (limited by the bit depth of the comb software) and 50 mHz, respectively. This indicates that the OFC remains consistently phase locked and reproduces the expected Allan deviation.

A measured Allan deviation of the ring-down time constant, τ, also a figure of merit of the stationarity of the measurement statistics for the spectrometer, can be found in Figure S5. We demonstrate an $\alpha_{min} \sim 2\times10^{-12}$ cm^{-1}, which is competitive with similar ultra-sensitive CRDS techniques [16-18]. Interestingly, the system maintains statistically stationary behavior for nearly an order-of-magnitude-longer measurement time than that previously reported for FS-CRDS [16]. This provides benefits for highly precise spectral measurements, because an entire molecular transition may be recorded within this time interval with a reasonable number of ring-down averages at each spectral point.

We also compared the integrated cavity transmission with and without the phase-lock and found that the lock resulted in a tenfold increase in laser coupling as determined by the integrated laser transmission. Although acquisition rates of 500 Hz have been demonstrated, optical losses in the EOM typically reduces this to 200 Hz, yielding a typical noise-equivalent absorption coefficient of ~10^{-11} cm^{-1}Hz$^{-1/2}$.

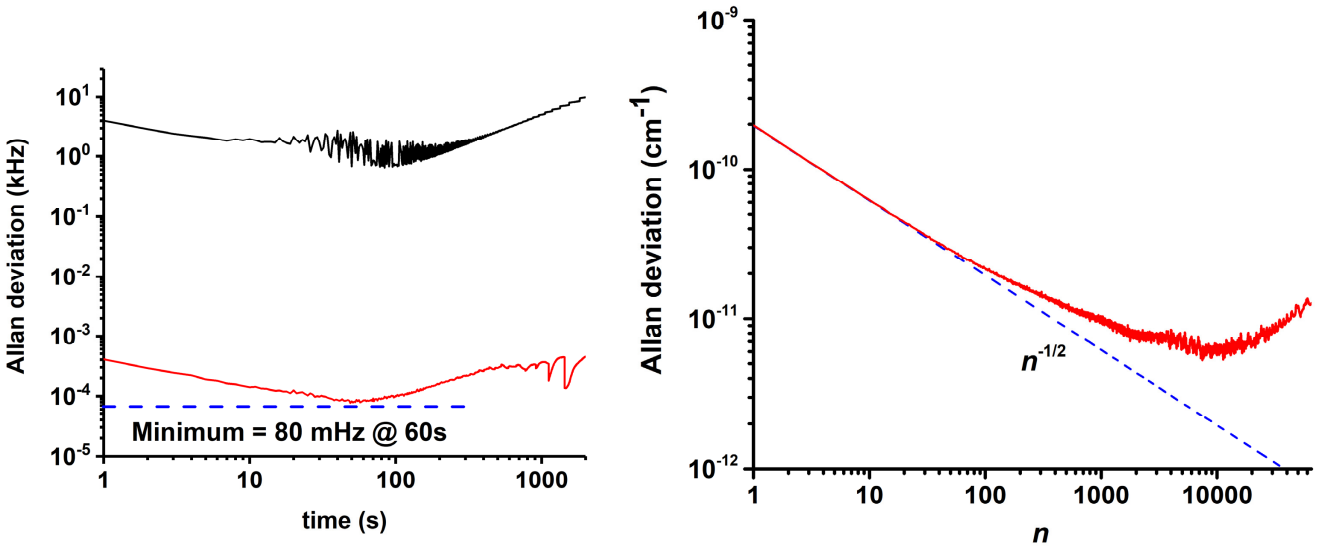

Fig. S5 (a) Allan deviations of the heterodyne beat signals between the free-running ECDL (black trace) and OFC, and the out-of-loop signal of the comb-locked ECDL (red trace) and OFC. The dashed line indicates the Allan deviation minimum. (b) Normalized Allan deviation, $\sigma_\tau/(c\tau^2)$, of the empty cavity decay time for n ring-down events. The dashed line is the idealized $n^{-1/2}$ averaging behavior.

9. Comparison to Literature

Several previous comb-linked studies have investigated various transitions in the (30012) ← (00001) band. A comparison of these previous results to the current work may be found in Table S1. Further discussion may be found in the main text.

Disclaimer

Certain commercial equipment, instruments, or materials are identified in this paper to specify the experimental conditions adequately. Such identification is not intended to imply recommendation or endorsement by the National Institutes of Standards and Technology, nor is it intended to imply that the materials or equipment identified are necessarily the best available for the purpose.

		P24e	P14e	P12e	P10e	R16e
This work	ν_0 (MHz)	189 680 512.8002(5)	189 955 768.0136(5)	190 008 170.1995(5)	190 059 681.7246(3)	190 667 021.4097(2)
Long et al [19]	ν_0 (MHz)	189 680 512.714(120)	189 955 767.968(60)	190 008 170.101(23)	190 059 681.670(60)	190 667 021.408(30)
	Deviation (kHz)	87	45	99	54	1.7
Truong et al [20]	ν_0 (MHz)		189 955 768.023(9)			
	Deviation (kHz)		-9			
Gatti et al [12]	ν_0 (MHz)		189 955 768.022(3)			
	Deviation (kHz)		-8.4			
Gotti et al [21]	ν_0 (MHz)			190 008 170.181(2)		
	Deviation (kHz)			19		
Rutkowski et al [22]	ν_0 (MHz)					190 667 024.2(7)
	Deviation (kHz)					-2792

Table S1 Transition frequencies ν_0 in this work and in the literature of the (30012) ← (00001) $^{12}C^{16}O_2$ vibrational band, along with the deviation from this work (Present minus Reference)

References

1. A. J. Fleisher, E. M. Adkins, Z. D. Reed, H. Yi, D. A. Long, H. M. Fleurbaey, and J. T. Hodges, "Twenty-Five-Fold Reduction in Measurement Uncertainty for a Molecular Line Intensity," Physical Review Letters **123**, 043001 (2019).
2. V. T. Sironneau and J. T. Hodges, "Line shapes, positions and intensities of water transitions near 1.28 µm," Journal of Quantitative Spectroscopy and Radiative Transfer **152**, 1-15 (2015).
3. T. M. Delahaye, S.E.; Reed, Z.D.; Lin, H.; J.T. Hodges, Sung, K.; Devi, V.M.; Warneke, T.; Spietz, P.; Tran, H., "Precise methane absorption measurementsin the 1.64µm spectral regionfor the MERLIN mission," J. Geophys. Res. **121**, 7360-7370 (2016).
4. I. E. Gordon, L. S. Rothman, C. Hill, R. V. Kochanov, Y. Tan, P. F. Bernath, M. Birk, V. Boudon, A. Campargue, K. V. Chance, B. J. Drouin, J. M. Flaud, R. R. Gamache, J. T. Hodges, D. Jacquemart, V. I. Perevalov, A. Perrin, K. P. Shine, M. A. H. Smith, J. Tennyson, G. C. Toon, H. Tran, V. G. Tyuterev, A. Barbe, A. G. Császár, V. M. Devi, T. Furtenbacher, J. J. Harrison, J. M. Hartmann, A. Jolly, T. J. Johnson, T. Karman, I. Kleiner, A. A. Kyuberis, J. Loos, O. M. Lyulin, S. T. Massie, S. N. Mikhailenko, N. Moazzen-Ahmadi, H. S. P. Müller, O. V. Naumenko, A. V. Nikitin, O. L. Polyansky, M. Rey, M. Rotger, S. W. Sharpe, K. Sung, E. Starikova, S. A. Tashkun, J. V. Auwera, G. Wagner, J. Wilzewski, P. Wcisło, S. Yu, and E. J. Zak, "The HITRAN2016 molecular spectroscopic database," Journal of Quantitative Spectroscopy and Radiative Transfer **203**, 3-69 (2017).
5. D. A. Long, Z. D. Reed, A. J. Fleisher, J. Mendonca, S. Roche, and J. T. Hodges, "High-Accuracy Near-Infrared Carbon Dioxide Intensity Measurements to Support Remote Sensing," Geophysical Research Letters **47**, e2019GL086344 (2020).
6. V. Malathy Devi, D. C. Benner, L. R. Brown, C. E. Miller, and R. A. Toth, "Line mixing and speed dependence in CO2 at 6348cm−1: Positions, intensities, and air- and self-broadening derived with constrained multispectrum analysis," Journal of Molecular Spectroscopy **242**, 90-117 (2007).
7. D. Jacquemart, R. Gamache, and L. S. Rothman, "Semi-empirical calculation of air-broadened half-widths and air pressure-induced frequency shifts of water-vapor absorption lines," Journal of Quantitative Spectroscopy and Radiative Transfer **96**, 205-239 (2005).
8. W. Q. Cai, T. E. Gough, X. J. Gu, N. R. Isenor, and G. Scoles, "Polarizability of CO2 studies in molecular beam laser Stark spectroscopy," Physical Review Letters **36**, 4722 (1987).
9. J. Lodewyck, M. Zawada, L. Lorini, M. Gurov, and P. Lemonde, "Observation and Cancellation of a perturing Stark shift in Sr optical clocks," IEEE Transactions of Ultrasonic Ferroelectric Frequency Control **59**, 411 (2012).
10. J. Burkart, T. Sala, D. Romanini, M. Marangoni, A. Campargue, and S. Kassi, "Communication: Saturated CO2 absorption near 1.6 µm for kilohertz-accuracy transition frequencies," The Journal of Chemical Physics **142**, 191103 (2015).
11. L. A. Rahn, R. L. Farrow, M. L. Koszykowski, and P. L. Mattern, "Observation of an Optical Stark Effect on Vibrational and Rotational Transitions," Physical Review Letters **45**, 620-623 (1980).
12. D. Gatti, T. Sala, R. Gotti, L. Cocola, L. Poletto, M. Prevedelli, P. Laporta, and M. Marangoni, "Comb-locked cavity ring-down spectrometer," The Journal of Chemical Physics **142**, 074201 (2015).
13. A. Shelkovnikov, R. J. Butcher, C. Chardonnet, and A. Amy-Klein, "Stability of the Proton-to-Electron Mass Ratio," Physical Review Letters **100**, 150801 (2008).
14. N. Bucalovic, V. Dolgovskiy, C. Schori, P. Thomann, G. Di Domenico, and S. Schilt, "Experimental validation of a simple approximation to determine the linewidth of a laser from its frequency noise spectrum," Appl. Opt. **51**, 4582-4588 (2012).
15. T. Okoshi, K. Kikuchi, and A. Nakayama, "Novel method for high resolution measurement of laser output spectrum," Electronics Letters **16**, 630-631 (1980).
16. H. Lin, Z. D. Reed, V. T. Sironneau, and J. T. Hodges, "Cavity ring-down spectrometer for high-fidelity molecular absorption measurements," Journal of Quantitative Spectroscopy and Radiative Transfer **161**, 11-20 (2015).
17. G. W. Truong, K. O. Douglass, S. E. Maxwell, R. D. van Zee, D. F. Plusquellic, J. T. Hodges, and D. A. Long, "Frequency-agile, rapid scanning spectroscopy," Nature Photonics **7**, 532 (2013).
18. J. Burkart, D. Romanini, and S. Kassi, "Optical feedback frequency stabilized cavity ring-down spectroscopy," Opt. Lett. **39**, 4695-4698 (2014).
19. D. A. Long, S. Wójtewicz, C. E. Miller, and J. T. Hodges, "Frequency-agile, rapid scanning cavity ring-down spectroscopy (FARS-CRDS) measurements of the (30012)←(00001) near-infrared carbon dioxide band," Journal of Quantitative Spectroscopy and Radiative Transfer **161**, 35-40 (2015).
20. G.-W. Truong, D. A. Long, A. Cygan, D. Lisak, R. D. v. Zee, and J. T. Hodges, "Comb-linked, cavity ring-down spectroscopy for measurements of molecular transition frequencies at the kHz-level," The Journal of Chemical Physics **138**, 094201 (2013).
21. R. Gotti, D. Gatti, P. Masłowski, M. Lamperti, M. Belmonte, P. Laporta, and M. Marangoni, "Conjugating precision and acquisition time in a Doppler broadening regime by interleaved frequency-agile rapid-scanning cavity ring-down spectroscopy," The Journal of Chemical Physics **147**, 134201 (2017).
22. L. Rutkowski, P. Masłowski, A. C. Johansson, A. Khodabakhsh, and A. Foltynowicz, "Optical frequency comb Fourier transform spectroscopy with sub-nominal resolution and precision beyond the Voigt profile," Journal of Quantitative Spectroscopy and Radiative Transfer **204**, 63-73 (2018).